

Research article

# Tunable mechanical properties of thermoplastic foams produced by additive manufacturing

Abdullah Alduais<sup>1</sup>, Sezer Özerinç<sup>1,2\*</sup>

<sup>1</sup>Department of Mechanical Engineering, Middle East Technical University, 06800 Ankara, Turkey

<sup>2</sup>Department of Micro and Nanotechnology, Middle East Technical University, 06800 Ankara, Turkey

Received 24 June 2022; accepted in revised form 4 October 2022

**Abstract.** Fused deposition modeling (FDM) is a versatile additive manufacturing technique for producing polymeric parts. Incorporating a foaming agent into the filament material enables the FDM-printing of thermoplastic foams, which opens up new possibilities for achieving desired mechanical property combinations. This study explored the process-property design space of FDM-printed polylactic acid (PLA) foams. Tensile and compression specimens were produced at a wide range of printing parameters using a commercial thermoplastic filament containing a foaming agent. Increasing the nozzle temperature and decreasing the filament feed rate increased the extent of foaming. Adjustment of the nozzle temperature, feed rate, and infill ratio controlled porosity over a density range of 0.24 to 1.17 g/cm<sup>3</sup>. Tuning of the mechanical properties over an order of magnitude was demonstrated, with elastic moduli ranging from 0.24 to 3.7 GPa and tensile strength ranging from 4.2 to 34.5 MPa. The mechanical behavior closely followed the Gibson-Ashby model predictions. Foaming filaments provide a new tool for tuning the mechanical response of FDM-printed parts to achieve unique combinations of mechanical properties that are not attainable through conventional methods.

**Keywords:** mechanical properties, additive manufacturing, fused deposition modeling, polymer foaming, polylactic acid

## 1. Introduction

Material extrusion is a low-cost and easy-to-use method for the manufacturing of prototypes as well as complex load-bearing components in small quantities. When the printed material is thermoplastic, the technique is commonly referred to as fused deposition modelling (FDM) or fused filament fabrication (FFF) [1].

The FDM process, schematically described in Figure 1, is based on the thermoplastic material's melting and extrusion through a heated nozzle. The printing head deposits the molten polymer in the desired locations by moving in the XY plane. Upon completing a layer, the build plate moves down incrementally, and the process is repeated [2].

The simplicity of the FDM process makes it a cost-effective and versatile alternative for manufacturing

complex geometries in small quantities. While earlier applications have been primarily focused on prototyping, recent advances in the process and filament material technology have enabled the use of FDM-produced parts for load-bearing and impact-absorbing components [3].

Due to their desirable rheological properties and low cost, polylactic acid (PLA) and acrylonitrile butadiene styrene (ABS) have been the most commonly used filament materials in FDM. On the other hand, there have been several advancements in materials for FDM. Some examples include polymer blends such as PLA/polyhydroxyalkanoate (PHA) for improved ductility, elastomeric filaments for producing compliant and hyperelastic components, and fiber-reinforced filaments for improved strength [4].

\*Corresponding author, e-mail: [ozerin@metu.edu.tr](mailto:ozerin@metu.edu.tr)

© BME-PT

Recent advances in filament fabrication technology have also enabled the production of foaming filaments. The unique nature of the foaming process during printing allows the spatial control of the porosity. The capability of printing polymeric foams and the direct control over their properties adds a new design parameter to the additive manufacturing of polymeric structures for achieving the desired combinations of stiffness, strength, and density [5].

In FDM printing of an in-situ foaming polymer, the chemical foaming agent in the filament forms gas bubbles triggered by the heating in the extrusion process [6–8]. The subsequent solidification of the printed thermoplastic provides a foam with a relatively uniform distribution of pores, analogous to the well-established foam extrusion process [9]. PLA samples produced by injection-molding foaming [10] and FDM-printed samples share similar closed-foam morphologies. Compared to microcellular injection molding [11], FDM printing with in-situ foaming tends to provide a higher number density of pores [6].

As opposed to the conventional manufacturing of polymeric foams, FDM enables the adjustment of the porosity on the fly through changes in the nozzle temperature or filament feed rate. The resulting ability to spatially control the porosity provides a unique opportunity to design mechanical responses that conventional manufacturing cannot achieve. FDM's capability of producing architected cellular structures [12, 13] complements this added feature of variable porosity, which offers a further degree of freedom in generating lightweight and compliant structures.

Thermal insulation and mechanical cushioning applications widely use conventional polymeric foams [14]. The development of superior polymeric foams, especially for functional and structural applications, is an active field of research [15]. The pore morphology and the density of foams are a complicated function of the polymer and precursor chemistry, as well as the dynamics of the cell nucleation, cell growth, and eventual stabilization of the structure through solidification [16, 17]. The mechanical response depends on the solid volume fraction and the general features of the ligament geometry, which has been widely studied through modeling [18] and experimental studies [19–21].

FDM of polymeric foams provides new possibilities for designing and manufacturing optimized structures for various applications. The foaming combined with the existing capability of FDM in producing

cellular structures can give hierarchical architectures at two different scales. Such structures enhance the performance of biomedical scaffolds [7, 22], and PLA's high biocompatibility and biodegradability make this route a readily applicable approach. In addition, the spatially tunable porosity enables the production of parts with variable stiffness, useful for implementing energy-absorbing structures and soft robotics [23].

The studies on the FDM printing of polymeric foams have focused on developing foaming technology and optimizing the synthesis process. A common approach has been to saturate the filament with CO<sub>2</sub>, followed by the in-situ foaming during 3D printing, demonstrated for polyethyleneimine (PEI) [24, 25], and PLA [26]. The second approach has been to post-process the non-porous FDM part by applying CO<sub>2</sub> gas-foaming [27, 28]. For the in-situ foaming method, the current understanding regarding the effect of FDM parameters on the mechanical performance of printed parts is quite limited.

Compared to the conventional manufacturing of polymeric foams, the in-situ foaming-based FDM process exhibits additional complications regarding the process parameters. FDM-produced parts' properties strongly depend on the nozzle temperature, raster orientation, build direction, and infill ratio. While the associated process-property relationships have been investigated for common filament materials such as PLA and ABS [4, 29, 30, 31], there has not been a similar investigation for the FDM of foaming filaments.

This work investigates the process-structure-property relationships for a commercially available foaming PLA filament. The study considers the effect of nozzle temperature, infill ratio, feed rate, and printing speed on the foaming characteristics, density, and strength of the produced parts. The results provide insight into the design space offered by the FDM printing of foaming polymers.

## 2. Experimental details

An Ultimaker 2+ FDM 3D printer (Ultimaker B.V., Utrecht, Netherlands) printed the specimens. The filament was the commercially available LW-PLA (Colorfabb, Belfeld, Netherlands) with a diameter of 2.85 mm and a density of 1.24 g/cm<sup>3</sup> [32]. The filament mainly consists of PLA and is designed to foam under certain printing conditions. While the manufacturer does not give detailed information about the filament formulation, a common approach is to saturate

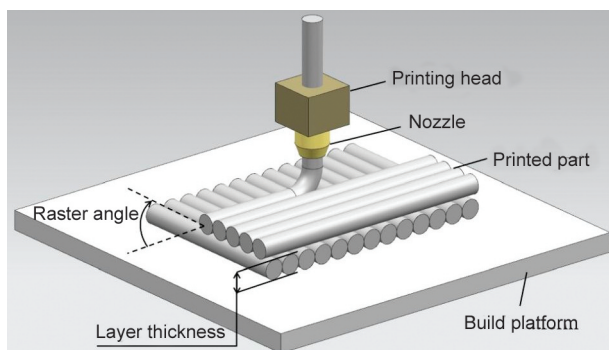


**Figure 1.** Schematic description of the fused deposition modeling (FDM) technique.

the filament with CO<sub>2</sub> or mix the filament with a chemical foaming agent, which facilitates in-situ foaming during printing [6, 24, 25].

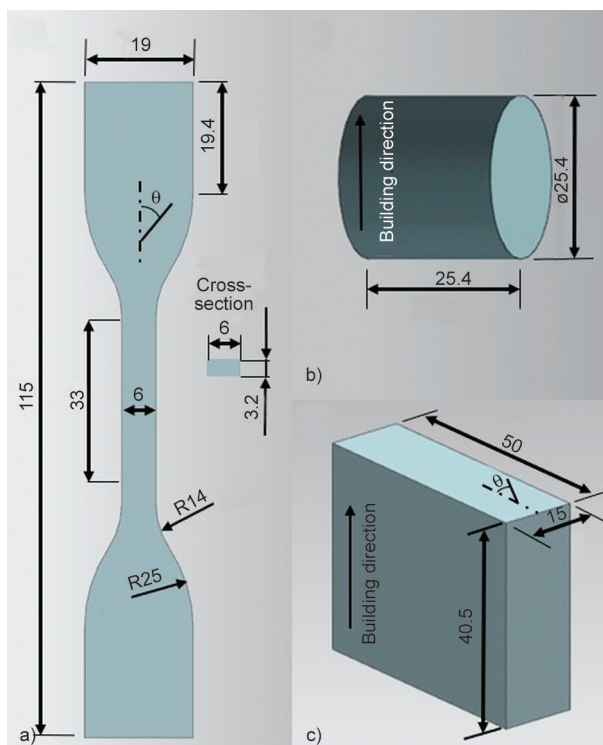
Figure 2 shows a summary of the test specimen geometries employed. The dog bone-shaped specimens were based on the Type 4 geometry of the ASTM D638 Standard Test Method for Tensile Properties [33]. Cylindrical specimens having a diameter and height of 25.4 mm were produced for compression testing according to ASTM D1621 Standard Test Method for Compressive Properties of Rigid Cellular Plastics [34]. The third geometry was a rectangular slab with varying printing parameters over the build direction for Shore A hardness testing, according to ASTM D2240 Standard Test Method for Rubber Property – Durometer Hardness [35].

Figure 1 shows a schematic description of the printing process and indicates some process parameters. Table 1 summarizes the printing parameters that are common to all specimens. The printing trajectory

**Table 1.** Printing parameters that are common for all tensile and compression specimens.

Parameter	Value
Filament diameter [mm]	2.85
Filament density [g/cm <sup>3</sup> ]	1.24
Nozzle diameter [mm]	0.4, 0.6*
Nozzle temperature [°C]	215–260*
Bed temperature [°C]	60
Layer thickness [mm]	0.2–0.7 for the parametric study, 0.45 elsewhere*
Infill pattern	±45°, except for the infill ratio study with grid pattern
Infill ratio [%]	25–100 for the parametric study, 100% elsewhere*
Inwall layers	3, except the infill ratio study that used 2
Top and bottom layers	Same as other layers

\*See Table 2 for further details on these parameters.



**Figure 2.** Schematic views of the specimen geometries. a) Tensile specimen. b) Compression specimen. c) Rectangular slab specimen with graded properties for Shore hardness measurements. All dimensions are in mm.

employed an alternating raster of  $\theta = \pm 45^\circ$ , as defined in Figure 2c. Other raster orientations were not considered as the primary focus of the study was on parameters that directly influence the foaming characteristics. The only exception was the grid raster type employed for the tensile specimens with varying infill ratios. At least five identical tension and compression specimens were printed for all printing parameter combinations.

The study systematically investigated the effect of nozzle temperature, layer thickness, feed rate, printing speed, and infill ratio through tension and compression tests. Table 2 summarizes the printing conditions utilized for this parametric study.

The rectangular slab specimen was printed using a nozzle temperature of 230 °C, layer thickness of 0.45 mm, printing speed of 45 mm/s, and infill ratio of 100%. The feed rate varied linearly from 20 to 100% in the build direction, according to the definition in Figure 2c.

A Zwick/Roell Z250 (ZwickRoell, Ulm, Germany) universal testing machine performed the tensile and compression tests at room temperature. The displacement rate was 5 mm/min for both cases. A Type-A hardness tester JIS (KORI SEIKI MFG, Tokyo,

**Table 2.** The printing conditions employed in the parametric study for tension, compression, and Shore hardness specimens.

Parameter under investigation	Range of values considered				Fixed parameters						
					ND* [mm]	NT* [°C]	LT* [mm]	FR* [%]	PS* [mm/s]	IR* [%]	IT*
NT [°C]	215	230	245	260	0.4	–	0.45	100	50	100	±45°
LT [mm]	0.2	0.35	0.5	0.7	0.6	230/245	–	100	50	100	±45°
FR [%]	100	75	50	25	0.4	230/245	0.45	–	50	100	±45°
PS [mm/s]	50	37.5	25	–	0.4	230/245	0.45	100	–	100	±45°
IR [%]	100	75	50	25	0.4	230	0.45	100	50	–	Grid
Shore hardness	Feed rate varied between 20 and 100%				0.4	230	0.45	–	50	100	±45°

\*ND: nozzle diameter, NT: nozzle temperature, LT: layer thickness, FR: feed rate, PS: printing speed, IR: infill ratio, IT: infill type.

Japan) performed the Shore hardness measurements with a tip of 0.79 mm diameter.

A Nikon Eclipse E200 (Nikon, Tokyo, Japan) optical microscope imaged the specimen fracture surfaces. There was no surface preparation before imaging. An FEI Quanta 400F (FEI, Oregon, USA) scanning electron microscope (SEM) imaged selected specimens at 20 kV. Before imaging, a desktop sputter coated the specimens with 10 nm Au-Pd.

### 3. Results and discussion

#### 3.1. Effect of nozzle temperature

We considered four different nozzle temperatures in the range of 215–260 °C, going beyond the recommendation by the manufacturer, 230–250 °C [32]. Figure 3 shows the tensile stress-strain data of the respective specimens. The results demonstrate the good repeatability of the measurements and the large influence of nozzle temperature on the mechanical behaviour. The tensile strength and the slope of the

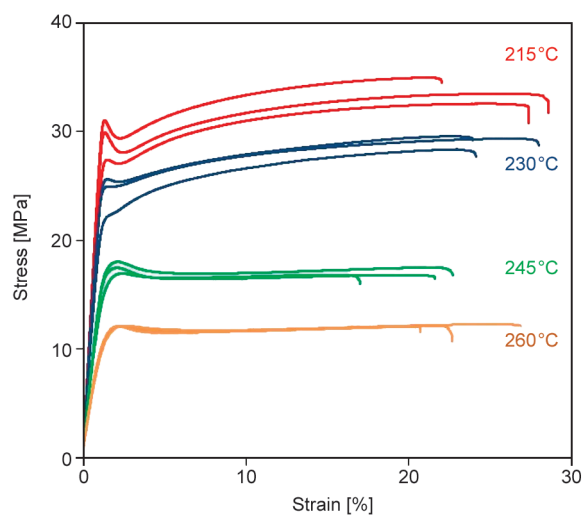


**Figure 3.** Representative tensile stress–tensile strain curves for specimens printed at different nozzle temperatures.

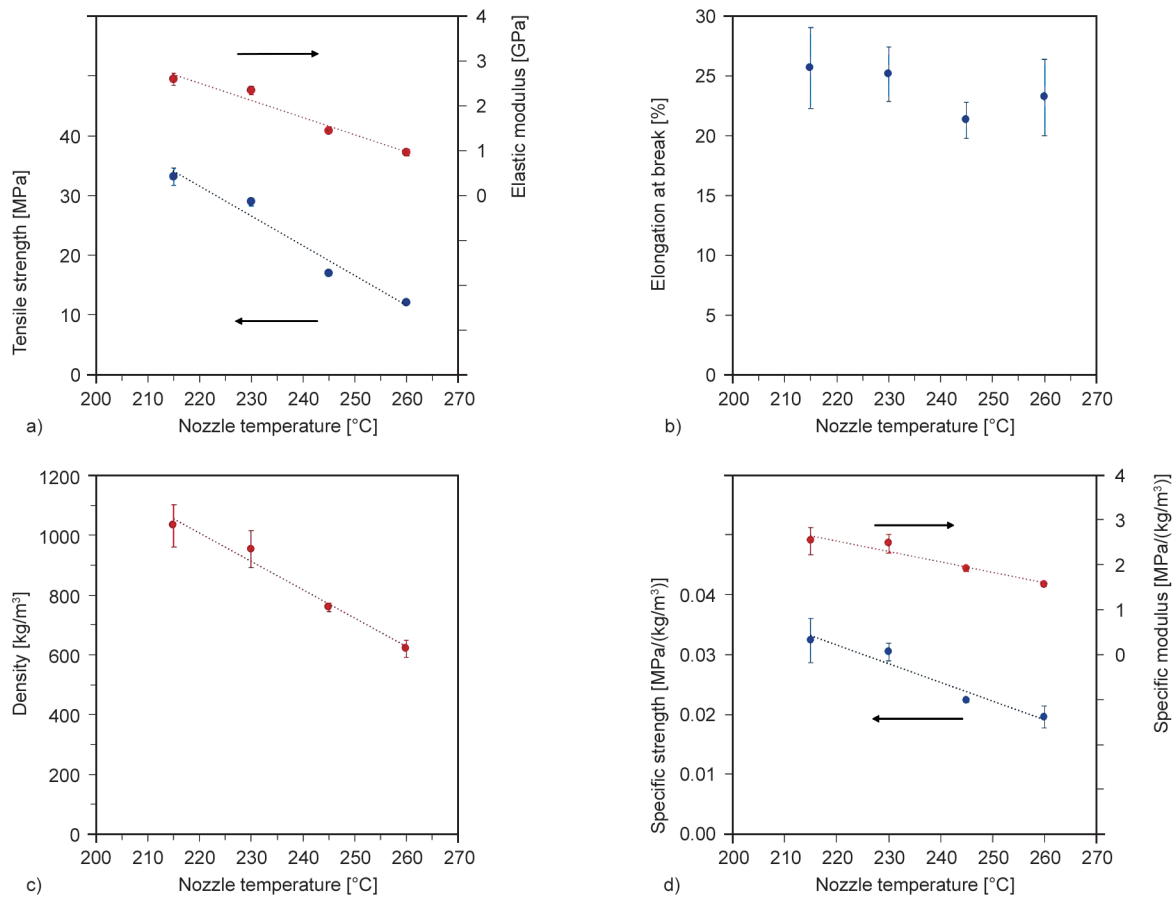
elastic response show a monotonic increase with decreasing nozzle temperature. Elongation at break remains relatively constant and does not exhibit an apparent variation.

Figure 4 shows the average mechanical properties, density, and density-specific mechanical properties as a function of nozzle temperature. Both tensile strength and elastic modulus monotonically decrease with increasing nozzle temperature. The nozzle temperature of 215 °C results in tensile strength of 33.2 MPa and an elastic modulus of 2.6 GPa. When the nozzle temperature reaches 260 °C, the strength and the modulus decrease almost by a factor of three and become 12.1 MPa, and 1.0 GPa, respectively (Figure 4a).

Elongation at break has a slightly decreasing trend with increasing nozzle temperature (Figure 4b). However, the variations are comparable to the standard deviation of the data. Density decreases monotonically with increasing nozzle temperature but at a slower rate than strength and elastic modulus.

Figure 5 shows optical microscope images of the fracture surfaces. The number density of pores increases with increasing nozzle temperature, indicating a rising extent of foaming. The fusion zones between printing lines contain fewer pores, and the fusion seems adequate, with no visible defects in either of the cases. The pores exhibit an almost perfect spherical morphology without any sign of flow-induced elongation.

Increasing nozzle temperature alters PLA's foaming characteristics. The diffusivity of the foaming agent rises with temperature and the bubble growth accelerates [36]. On the other hand, the solubility of the foaming agents usually gets lower with temperature, decreasing the number density of pores [36]. The overall effect is a rise in the porosity with temperature,



**Figure 4.** Effects of nozzle temperature on the density and the mechanical properties. a) Tensile strength and elastic modulus, b) elongation at break, c) density, and d) specific strength and specific modulus. The error bars represent one standard deviation.

as the increase in the bubble size is more pronounced than the decrease in the number density.

The variations in the porosity and the pore characteristics dramatically influence the mechanical properties. The density measurements (Figure 4c) and the microscope images (Figure 5) provide evidence for the monotonic rise of foaming with increasing nozzle temperature. A rising number density of pores decreases the apparent load-bearing area and reduces the strength and modulus, in agreement with the measurements. The decrease in strength is more pronounced than the elastic modulus due to the stress concentration sites introduced by the pores. A qualitative inspection of Figure 5 suggests a more rapid increase in foaming from 230 to 245 °C, which is also reflected in the measurement results presented in Figure 4.

Nozzle temperature affects the mechanical properties of non-foaming FDM-produced parts to a smaller extent. In FDM, increasing nozzle temperature increases the heat transfer to the deposition zone, which improves the quality of fusion between printed lines and layers [4, 37]. As a result, voids and gaps

that might result from poor fusion disappear, and the strength rises. However, the effect of the quality of fusion on strength is usually within 10% for 100% infill parts with quasi-isotropic raster conditions [4]. In our case, the microscope images demonstrate a good fusion between the layers even for the lowest nozzle temperature of 215 °C, eliminating the possibility of a pronounced fusion-based effect.

Lastly, nozzle temperature can also affect the printed part's crystallinity, potentially affecting the mechanical properties. For example, an increase in the nozzle temperature causes a higher cooling rate, which reduces the PLA crystallinity in PLA/PHA blend filaments [29]. However, the findings so far in the literature suggest that the crystallization-induced effects on mechanical properties are negligible in most cases. Furthermore, our DSC (data not shown here) analysis showed that the crystallinity does not vary considerably between the filament and the printed specimens for different nozzle temperatures. In addition, the specimen surfaces exhibited Fourier-transform infrared spectroscopy (FTIR) spectra that are

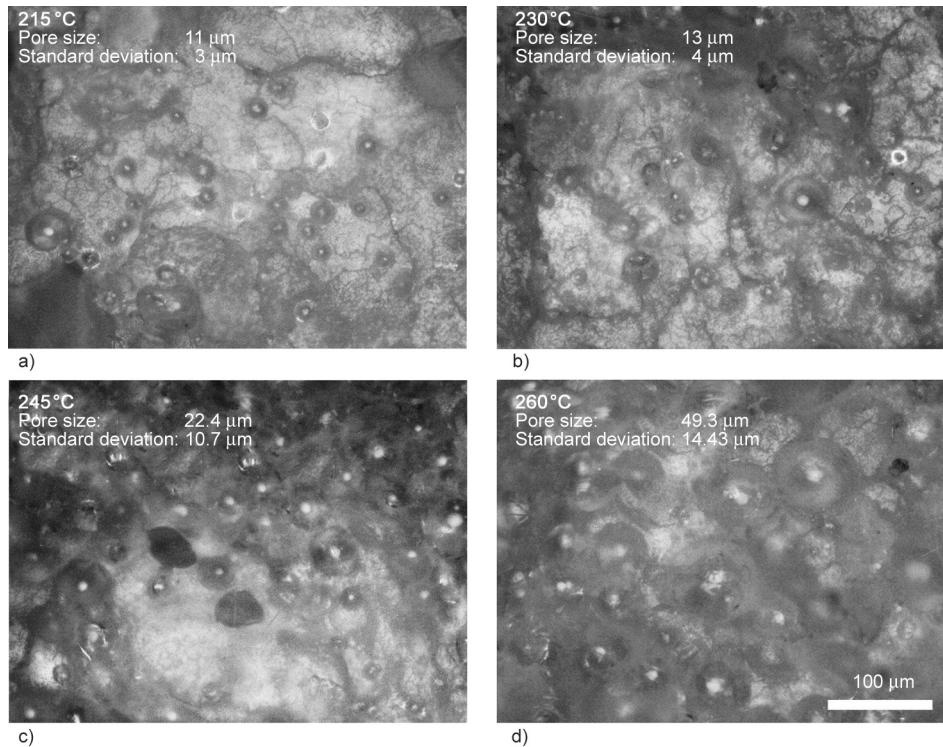


**Figure 5.** Optical microscope images of the printed specimens as a function of nozzle temperature. a) 215 °C, b) 230 °C, c) 245 °C, and d) 260 °C. The average pore size and its standard deviation is indicated for each case.

virtually the same as that of pure PLA, suggesting that there are no significant changes in the composition of the specimen surface (data not shown here). Therefore, we conclude that the foaming behavior is the primary cause of the observed mechanical properties variations.

As the specimens exhibit a wide range of densities, considering the specific strength and modulus values is helpful for better understanding the trends. The corresponding data in Figure 4d demonstrates that the specific strength and modulus decrease as the nozzle temperature increases and the density decreases. The drops in strength and modulus are more significant beyond 230 °C, suggesting that the pores' interaction and coalescence play a role in further weakening the porous structure [38].

### 3.2. Effect of filament feed rate

The filament feed rate defines the filament flow rate into the printing head. Most FDM printers automatically adjust the feed rate through their feeder mechanism to ensure continuous filling of the printing trajectory for a given nozzle diameter, printing speed, and layer thickness. The feed rate is usually defined in percentages, where 100% corresponds to the default flow rate that ensures continuous and void-free printing. While printing with conventional filaments,

the default feed rate of 100% does not need further adjustments. However, for the printing of the foaming PLA, feed rate becomes a very powerful tool to tune the extent of foaming. Figure 6 shows the four feed rates considered in this part and the corresponding flow rates calculated by measuring the total filament consumption and printing time in a build.

Figure 7 shows specimens' density and mechanical properties as a function of feed rate for two different

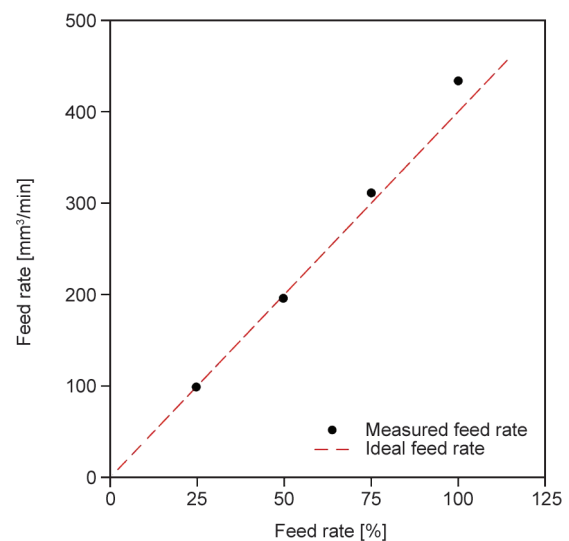


**Figure 6.** Relationship between the feed rate and measured filament flow rate for a nozzle diameter of 0.4 mm and a printing speed of 50 mm/s.

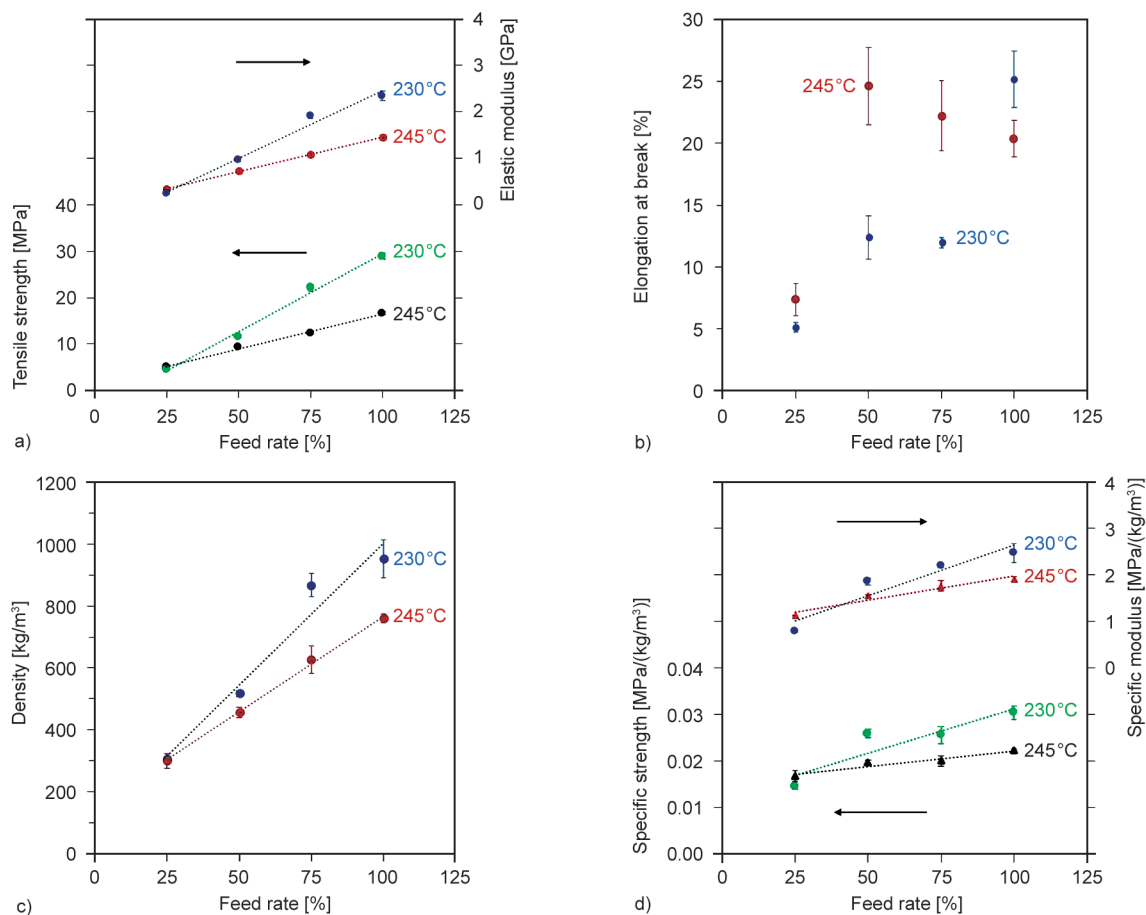


**Figure 7.** Effects of feed rate on the density and the mechanical properties. a) Tensile strength and elastic modulus, b) elongation at break, c) density, d) specific tensile strength and elastic modulus. Each plot shows the results for two different nozzle temperatures of 230 and 245 °C.

nozzle temperatures, namely, 230 and 245 °C. Density, tensile strength, and elastic modulus increase sharply as the feed rate increases for both cases of nozzle temperatures. For the case of 230 °C, the dependence of the properties on feed rate is more pronounced. As the feed rate increases from 25 to 100%, tensile strength increases by a factor of about 6.5, and the rise in the elastic modulus reaches almost an order of magnitude.

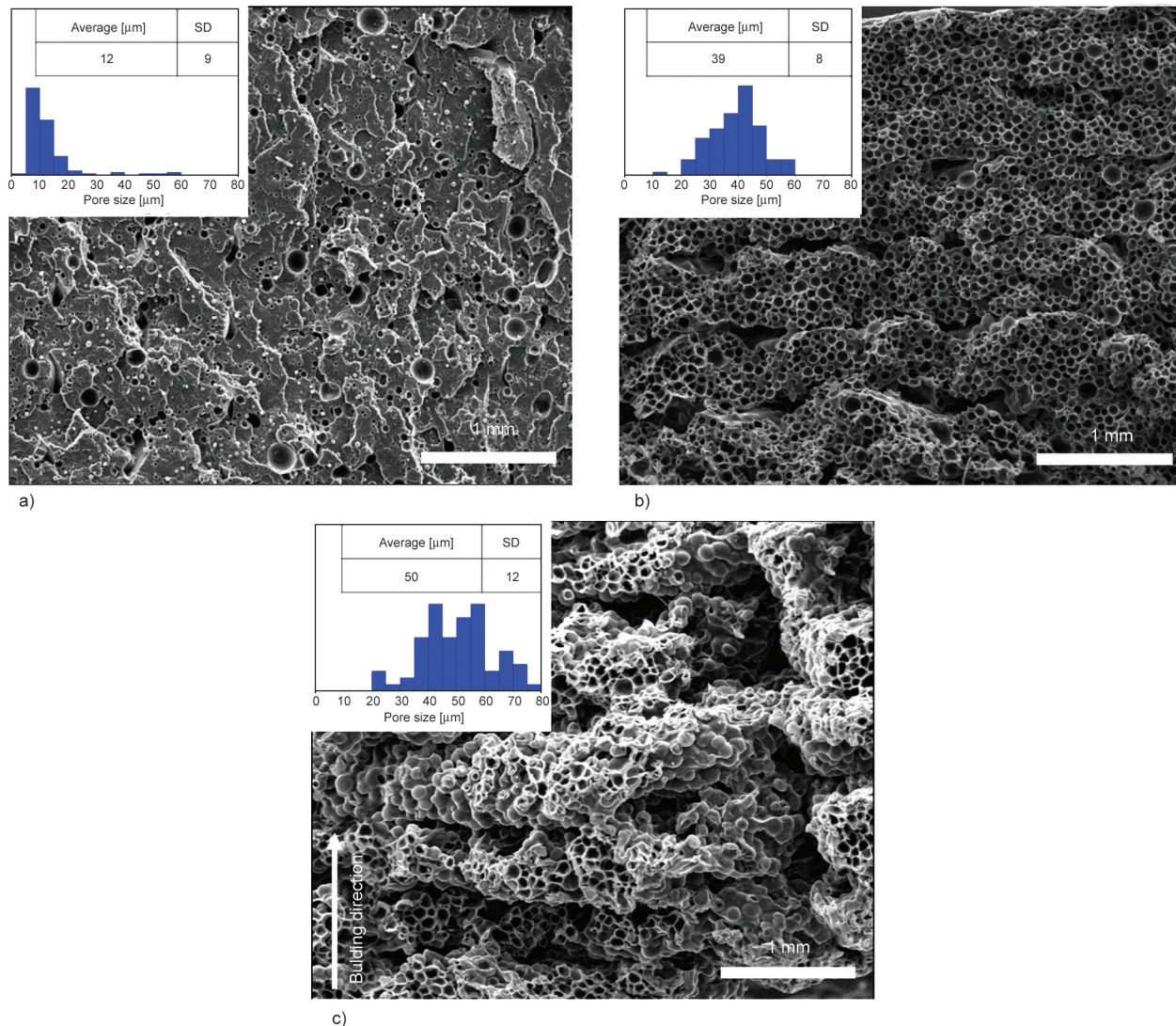
Elongation at break varies with feed rate differently for the nozzle temperatures of 230 and 245 °C. At 230 °C, elongation at break improves as the feed rate increases. For 245 °C, the elongation at break is around 25% for feed rates of 50% and higher and then exhibits a rapid drop to below 10% for the feed rate of 25%.

Figure 8 shows SEM images of the fracture surfaces of selected specimens printed at different feed rates. As the feed rate decreases, the number density of pores increases, and the layer interfaces start showing some gaps and defects.

Feed rate has a dramatic effect on the density and mechanical properties of the specimens. A low feed rate increases the travel time of the polymer through the hot zone and provides extra time for further gasification and porosity formation [39]. The resulting porosity reduces the printed parts' density and load-bearing capacity.

The effect of feed rate on density and mechanical properties is more severe for the nozzle temperature of 230 °C. Figure 7d shows the specific strength and modulus, indicating that even the density-normalized data depends on the nozzle temperature. For a given feed rate, 245 °C specimens show inferior specific properties. These observations agree with the adverse effect of nozzle temperature on the specific properties discussed in the previous section (see Figure 4d).

Elongation at break data shows a more complicated trend, which can be understood by considering the effect of nozzle temperature on the quality of fusion. Especially for the 50 and 75% feed rates, the nozzle temperature of 245 °C provides a considerably higher



**Figure 8.** SEM images of the fracture surfaces of selected specimens printed by using different feed rates of a) 100%, b) 50%, and c) 25%. Nozzle temperature is 230 °C. SD: stands for standard deviation.

ductility than those of 230 °C. The higher resistance of 245 °C specimens to fracture is likely to result from the superior fusion between printing lines and layers at this temperature [40, 41]. The dependence on nozzle temperature diminishes at the lowest and highest feed rates due to the dominating effects of excess porosity and excess material flow, respectively. For example, at a feed rate of 100%, the 230 °C specimen does not exhibit any apparent lack of fusion, as shown in Figure 8a. As a result, the effect of nozzle temperature on the elongation at break becomes small.

The increasing extent of foaming with decreasing feed rate can be attributed to the hydrostatic pressures involved in the process. As the filament material goes through the heating section and the nozzle, the diameter of the polymer flow cross-section decreases almost by an order of magnitude, resulting in a pressure rise. This pressure is highest in the case of 100% feed

rate, which hinders the expansion of the gas bubbles. A decrease in the feed rate is analogous to a reduction in the flow rate of a liquid through a channel, which reduces the pressure build-up in the heated section. As a result, the gas bubbles expand more quickly, resulting in a more significant fraction of porosity.

For the wide range of feed rate values considered in this study, the print quality remained satisfactory, which makes feed rate an excellent parameter to tune the porosity on the fly. As opposed to other parameters such as nozzle temperature, layer thickness, and infill ratio, feed rate does not cause any ‘side-effects’ that alter the resolution or quality of the print.

### 3.3. Effect of printing speed

Printing speed refers to the velocity magnitude of the nozzle during printing. Figure 9 shows the density and mechanical properties of the specimens as a

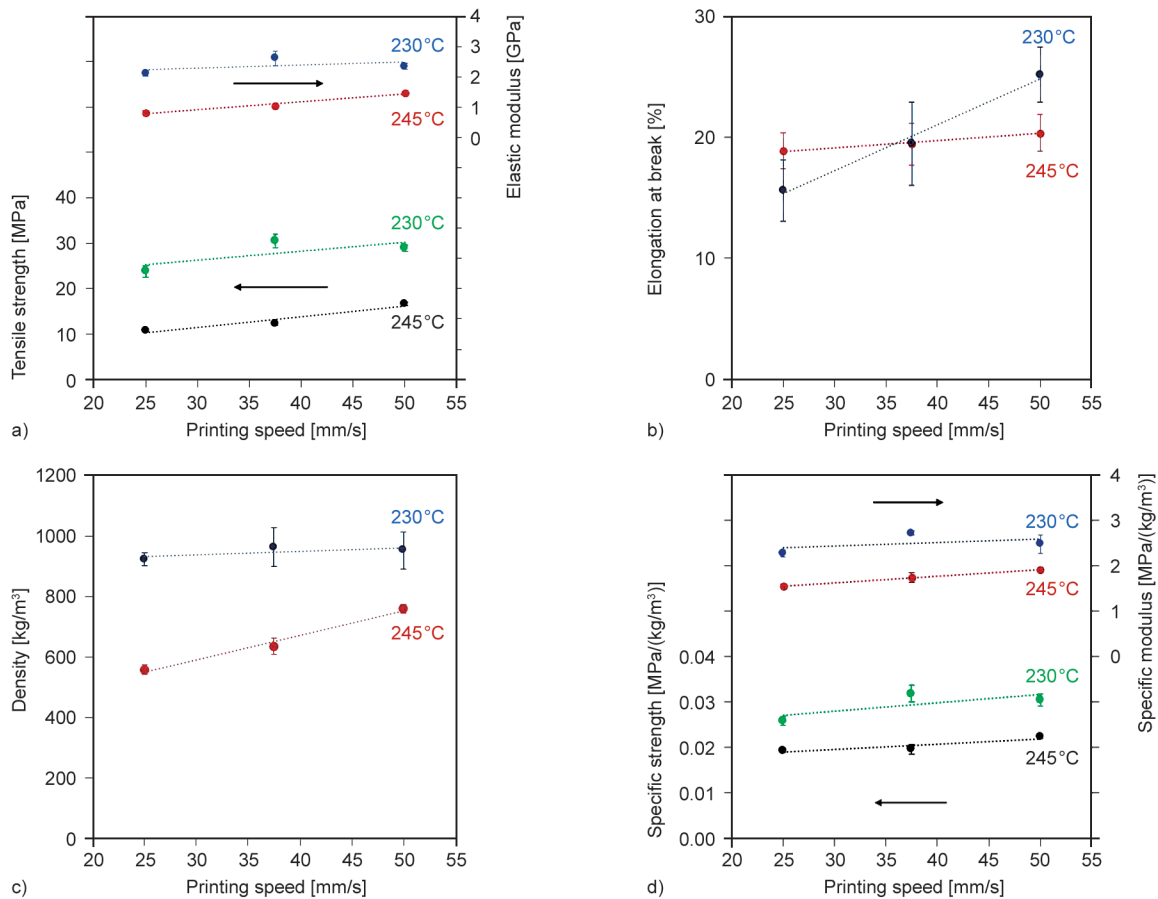


**Figure 9.** Effects of printing speed on the density and the mechanical properties. a) Tensile strength and elastic modulus, b) elongation at break, c) density, and d) specific tensile strength and specific elastic modulus.

function of printing speed, considered for two nozzle temperatures.

Overall, the printing speed does not significantly influence the mechanical properties. The only major trends are an increase in the density with increasing printing speed for the case of 245 °C and an increase in the elongation at break with increasing printing speed for the case of 230 °C.

As printing speed decreases, the filament stays longer in the heating section, promoting foaming and decreasing density. At 230 °C, the lower rate of the foaming reaction is insufficient to cause a strong dependence on printing speed. The small increase in elongation at break with printing speed can be explained by the slight increase in the density and accompanying reduction in the porosity, reducing the occurrence of stress concentration sites.

Printing speed is not a major parameter for tuning the foaming, which renders it useful for controlling other features. For example, the compromise between manufacturing rate and build quality can be the primary focus for optimizing the printing speed in practical applications.

### 3.4. Effect of infill ratio

Infill ratio is one of the most commonly varied parameters in additive manufacturing to establish a compromise between printing time, weight, and strength. A lower infill ratio implies shorter printing times and lower weight at the expense of lower strength. The resulting cellular geometry often introduces stress concentrations, leading to low elongations at break [42]. In practice, most FDM-produced parts are covered with a 100% infill shell to improve structural rigidity and provide a smooth and gapless surface for proper functionality. In this study, however, we considered tensile specimens without top and bottom shells to better understand the effect of the infill ratio. The infill pattern choice was grid (see Figure 11), one of FDM's most commonly used patterns.

Figure 10 shows the density and the mechanical properties of specimens printed at different infill ratios. As the infill ratio increases, the density and the mechanical properties show an increasing trend. 100% infill ratio provides the highest tensile strength and elastic modulus of 22.1, and 2073 MPa, respectively. Elongation at break values are considerably

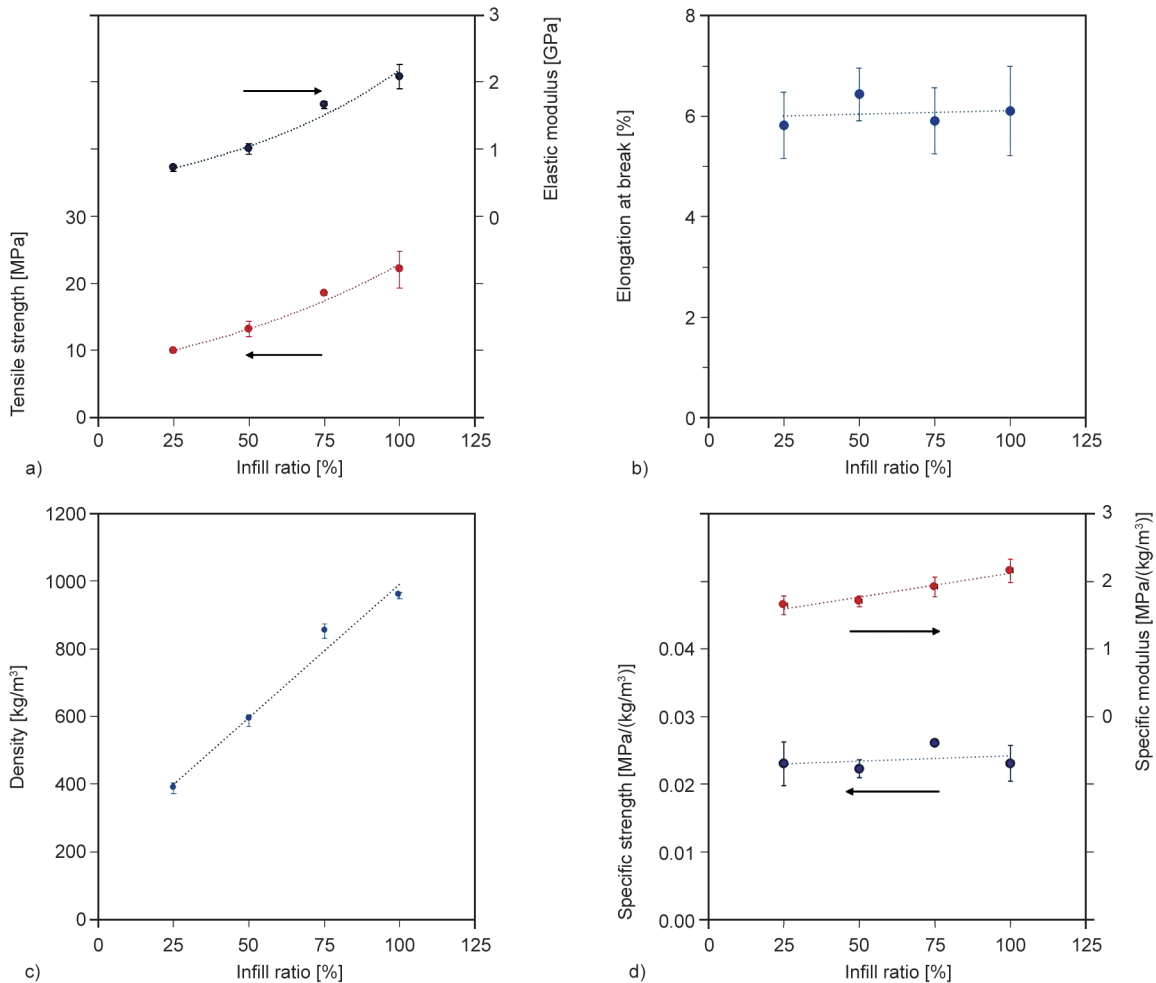


**Figure 10.** Effects of infill ratio on the density and the mechanical properties. a) Tensile strength and elastic modulus, b) elongation at break, c) density, d) specific tensile strength and specific elastic modulus.

lower than those measured in the previous sections, around 6% for all infill ratios.

Low elongation at break is a common feature of low infill ratio specimens. The stress concentrations due

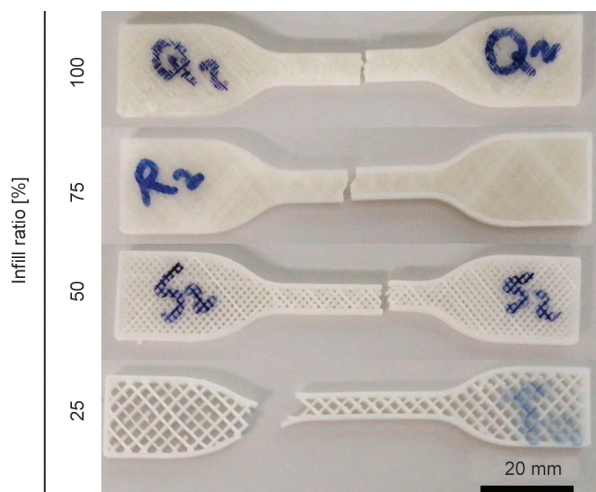


**Figure 11.** Photographs of selected specimens after testing with different infill ratios.

to the grid pattern are the primary reason for the premature failure. On the other hand, the 100% infill ratio specimen exhibiting a similarly low elongation requires a separate explanation. For 100% infill, the raster employed a grid pattern different from the  $\pm 45^\circ$  alternating layers employed for the rest of the study. We attribute the low elongation to the grid pattern that increases the likelihood of poor fusion and defects in a solid print. Further investigation of the effect of different printing patterns can give more insight, which has been beyond the scope of this work.

### 3.5. Effect of layer thickness

The layer thickness has a relatively smaller effect on the mechanical properties within the range of process parameters considered in this study. The results did not show clear trends; we only provide some key values here. For the nozzle temperature of 230 °C, 0.5 mm layer thickness yielded the highest tensile strength and elastic modulus of 33.3 MPa, and

3.14 GPa, respectively. On the other hand, 0.35 mm layer thickness provided the largest elongation at break (30%). At the higher nozzle temperature of 245 °C, 0.7 mm layer thickness yielded the best results with a tensile strength of 22.5 GPa and an elastic modulus of 2.08 GPa. Changing the layer thickness did not affect the density of the specimens, irrespective of the nozzle temperature.

The results suggest that tuning the layer thickness can optimize the surface quality, dimensional accuracy, and printing time, similar to the FDM printing with conventional filaments [2, 7, 43].

### 3.6. Overview of the design space

Table 3 compares the results with the key properties of PLA foams produced by injection molding [11, 44] and 3D printing [8] reported in the literature. Injection-molded parts can exhibit a wide range of porosities and mechanical properties depending on the implementation of the foaming agent and the process parameters. The example data taken from our work show that the mechanical properties of FDM-produced PLA foams are comparable to those of injection-molded parts, demonstrating the technology’s suitability for use in applications.

At a similar porosity level, FDM-produced specimens’ tensile strength and ductility were lower than those of injection molded specimens, possibly due to the additional fusion defects that FDM introduces. As the average pore size and its variation tend to be larger for injection molded specimens [44], a direct comparison is difficult, and future work is needed in this regard.

Figure 12 summarizes all mechanical property measurements as a function of density. The figure also in-

cludes the mechanical properties of a non-foamed specimen (nozzle temperature = 200 °C) produced by the same LW-PLA filament [45] and an FDM-produced conventional pure PLA specimen [46]. This comparison shows that the pure PLA specimen from the literature provides considerably higher strength than the foamed specimens. Examining the specific strength–density curve indicates that the higher strength of pure PLA is beyond the density’s contribution to strength. On the other hand, the elastic modulus of the pure PLA specimen is comparable to our specimens, suggesting that the pores and defects in the foamed specimens weaken the load-bearing capacity.

The data demonstrates the general trends in strength and modulus as a function of density that is common to all printing conditions. Tensile strength and elastic modulus increase with density (Figures 12a and 12b). The rate of increase in the mechanical properties amplifies with increasing density, and the scatter in the data widens accordingly. Specific strength also improves with density in general (Figure 12c). Especially for densities around 1000 kg/m<sup>3</sup>, specimens with similar densities can yield considerably different specific strengths, depending on the corresponding printing conditions. Overall, 230 °C nozzle temperature provides superior performance in absolute and specific strength. Tensile strength and elastic modulus are linearly proportional for most of the data, as shown in Figure 12d.

The entire data for each mechanical property follows a curve with a relatively narrow scatter, suggesting that the density, in fact, the porosity, is the primary parameter that governs the mechanical behavior of

**Table 3.** A comparison of the findings of this study with injection molded and FDM-produced specimens reported in the literature [8, 11, 44].

Reference	[44]	[11]	[8]	This study	
Production method	IM*	IM*	FDM	FDM	FDM
Nozzle temperature [°C]	170	180	215	230	230
Feed rate [%]	–	–	95	100	50
Infill ratio [%]	–	–	100	100	100
Mold temperature [°C]	25	10	–	–	–
Screw speed [rpm]	400	100	–	–	–
Elastic modulus [GPa]	0.91	1.46	1.89	2.34	0.96
Tensile strength [MPa]	25.1	33.6	31.2	28.9	11.5
Elongation at break [%]	43	30	–	25	12
Porosity [%]	28	–	–	24	56
Pore density [#cm <sup>3</sup> ]	0.48 · 10 <sup>6</sup>	0.23 · 10 <sup>8</sup>	–	0.16 · 10 <sup>8</sup>	0.8 · 10 <sup>6</sup>
Average pore size [µm]	90	120	–	14	40

\*IM: injection molding

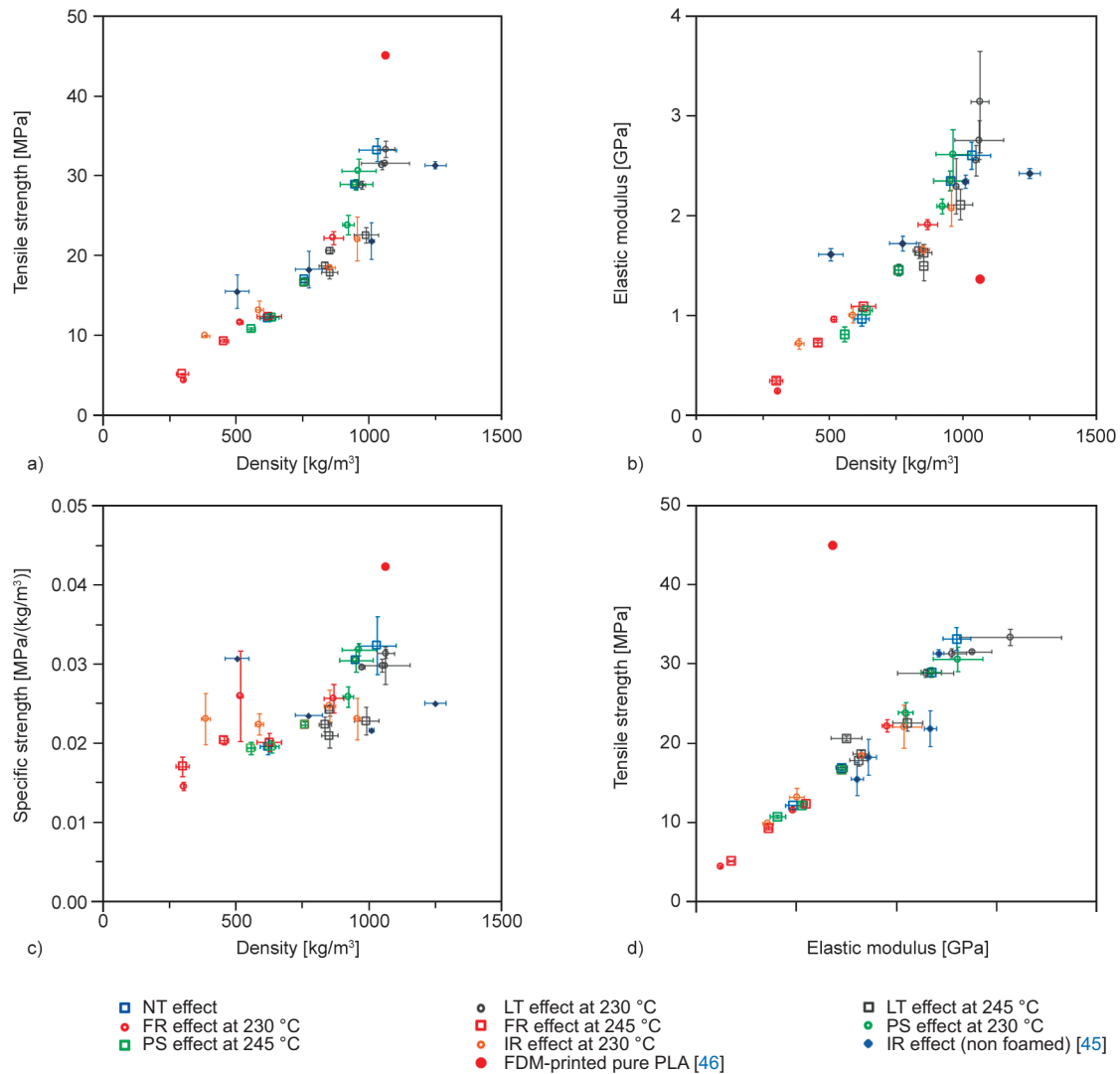


**Figure 12.** A summary of all mechanical property data. a) Tensile strength vs. density, b) elastic modulus vs. density, c) specific strength vs. density, and d) strength vs. elastic modulus. Each data point shows the average properties for a given combination of printing parameters. The printing parameters for non-foamed samples were nozzle temperature of 200 °C, raster angle of  $\pm 45^\circ$ , and layer height of 0.2 mm, and the infill ratio of the conventional PLA sample was 100% [45, 46].

the foaming PLA. In other words, the influence of process parameters on the mechanical properties is mainly through a change in the porosity. The effects of fusion defects and crystallinity are of secondary importance, supporting the previous discussion in Section 3.1.

The results show that porosity can be tuned by controlling a wide range of parameters, including nozzle temperature, feed rate, printing speed, layer thickness, and infill ratio. Most of these parameters also alter other features of the build at the same time. For example, increasing nozzle temperature improves the fusion between the layers, layer thickness affects the z-resolution of the build and the surface roughness, and printing speed would impact build quality,

manufacturing speed, and cost. Feed rate, on the other hand, only affects the porosity and does not influence the other feature significantly, making it the ideal choice for controlling the foaming. Controlling the feed rate for tuning foaming also provides the advantage of quickly adjusting the foaming spatially over the part. In contrast, on-the-fly adjustment of the nozzle temperature or the layer thickness is not as practical.

In summary, the findings suggest that 230 °C nozzle temperature is an effective value providing high specific strength. After this selection, the layer height and printing speed should be adjusted according to the requirements of the print, such as build quality and time restrictions. Then, the feed rate will provide

control over the extent of foaming. Lastly, the infill ratio and raster pattern can be used to adjust the weight of the printed part further.

As the study does not explore all possible combinations of printing parameters, the statements here are the implications of the existing data rather than conclusions, which would require a more comprehensive exploration of the entire design space. Such a future study should also investigate possible synergistic effects, such as how the impact of feed rate might change as a function of nozzle temperature and layer height.

The data for specimens with different infill ratios agree well with the porous specimens printed with 100% infill for a given density. Infill ratio tunes the density through a macroscale architected porosity, whereas the porous specimens achieve density control by foaming. The results suggest that foaming PLA printing is an excellent alternative to the conventional low-infill printing frequently used to reduce printing times, material consumption, and weight.

The Gibson-Ashby model is a useful and simple approach to predicting the mechanical properties of cellular materials and foams. The model predicts the elastic modulus and strength of the cellular structures as follows in Equations (1) and (2) [18]:

$$\frac{E_F}{E_S} = \varphi^2 \cdot \left(\frac{\rho_F}{\rho_S}\right)^2 + (1 - \varphi) \cdot \left(\frac{\rho_F}{\rho_S}\right) \quad (1)$$

$$\frac{\sigma_F}{\sigma_S} = 0.55 \cdot \left(\frac{\varphi \cdot \rho_F}{\rho_S}\right)^{1.5} + (1 - \varphi) \cdot \left(\frac{\rho_F}{\rho_S}\right) \quad (2)$$

where  $E$  is the elastic modulus,  $\sigma$  is the strength, and  $\varphi$  is a fitting parameter. Subscripts  $S$  and  $F$  refer to the fully solid and foamed specimens, respectively.

Figure 13 shows the elastic modulus and strength predictions of the Gibson-Ashby model using the properties of solid PLA from the literature [47] and compares the predictions with our data. The prediction curve exhibited a high coefficient of determination and low standard deviation, as indicated in the figures. The fitting constant,  $\varphi$ , is determined as 0.85 for both curves, in agreement with the literature values reported for polyurethane foams in the range of 0.8–0.85 [20, 48].

### 3.7. Compression testing

Compression testing of specimens provided further insight into the mechanical behavior of foaming PLA. We focused on specimens with varying feed rates, the simplest and most effective parameter to tune the porosity.

Figure 14a shows representative compressive stress-strain curves of specimens printed at different feed rates. The curves exhibit a linear-elastic regime, followed by a stress plateau and a second rise in stiffness, respectively. The slope of the elastic response and the magnitude of the stress plateau increase with increasing feed rate.

The stress-strain curves exhibit the typical characteristics of foams under compression. After the initial nearly-linear elastic response, the ligaments and surfaces surrounding the pores buckle, which reduces the load-bearing capacity. With further compression,

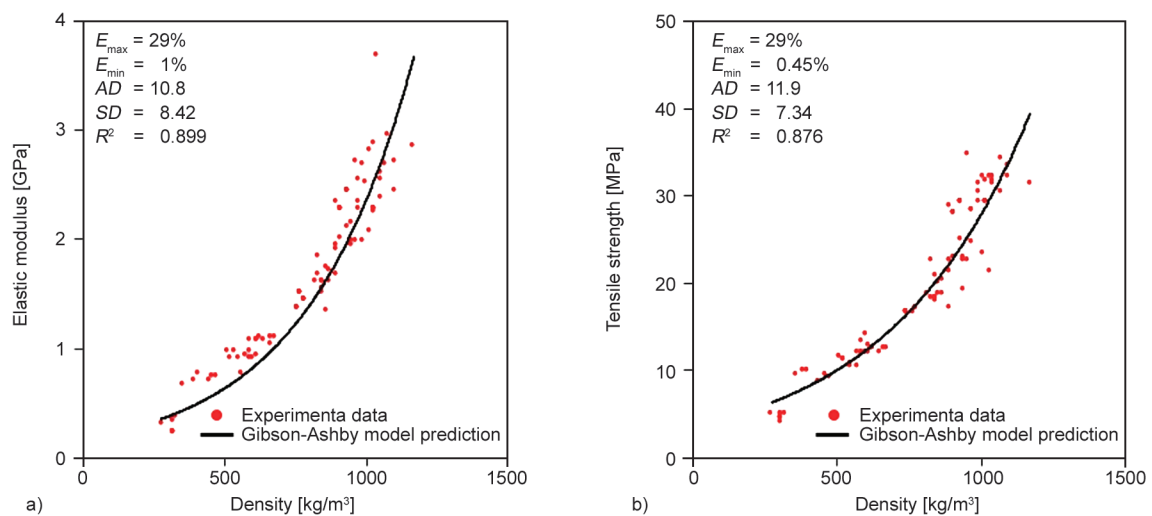


**Figure 13.** A comparison of all mechanical property data and Gibson-Ashby model predictions. a) Elastic modulus and b) tensile strength.  $E_{\max}$  and  $E_{\min}$ : the maximum and minimum percent difference respectively.  $AD$ : average difference.  $SD$ : standard deviation.  $R^2$ : coefficient of determination.

buckling and collapse propagate to the remainder of the specimen at a relatively constant stress level. As the collapse of the structure nears completion, deformations in the solid zones become more pronounced, which increases the measured stiffness. As the feed rate decreases, the porosity increases, and the onset of this stiffness rise is postponed to higher compressive strains.

Figures 14b, and 14c represent the density and the compressive mechanical properties as a function of feed rate for 230 °C nozzle temperature. Compressive strength corresponds to the local peak in the stress-strain curves right after the linear deformation segment. Density, compressive strength, and elastic modulus increase rapidly by increasing the feed rate. As the feed rate increases from 25 to 75%, the elastic modulus and compressive strength increase by factors of 13.3 and 9.5, respectively.

Figure 14d shows photographs of the compression specimens after testing. 100% feed rate specimen does not show any obvious damage upon a compression

exceeding 60% strain. As the feed rate decreases to 75 and 50%, the irreversible damage becomes more pronounced. In fact, 25% specimen shows little recovery upon unloading. All specimens apart from the 100% feed rate case show some delamination-like failure. Delamination planes are perpendicular to the build direction, suggesting that the fusion between layers is weaker than the fusion between adjacent printing lines.

### 3.8. Shore hardness measurements

The last part of the mechanical analysis was performed on a printed rectangular block with varying porosity over its build direction to demonstrate the foaming PLA's capability to generate structures with graded morphology. Decreasing the feed rate incrementally after the completion of each layer tuned the porosity in the build direction.

Figure 15 shows the Shore hardness measurements as a function of the build length and a photograph of the specimen. Shore hardness is 54.7 for the layers

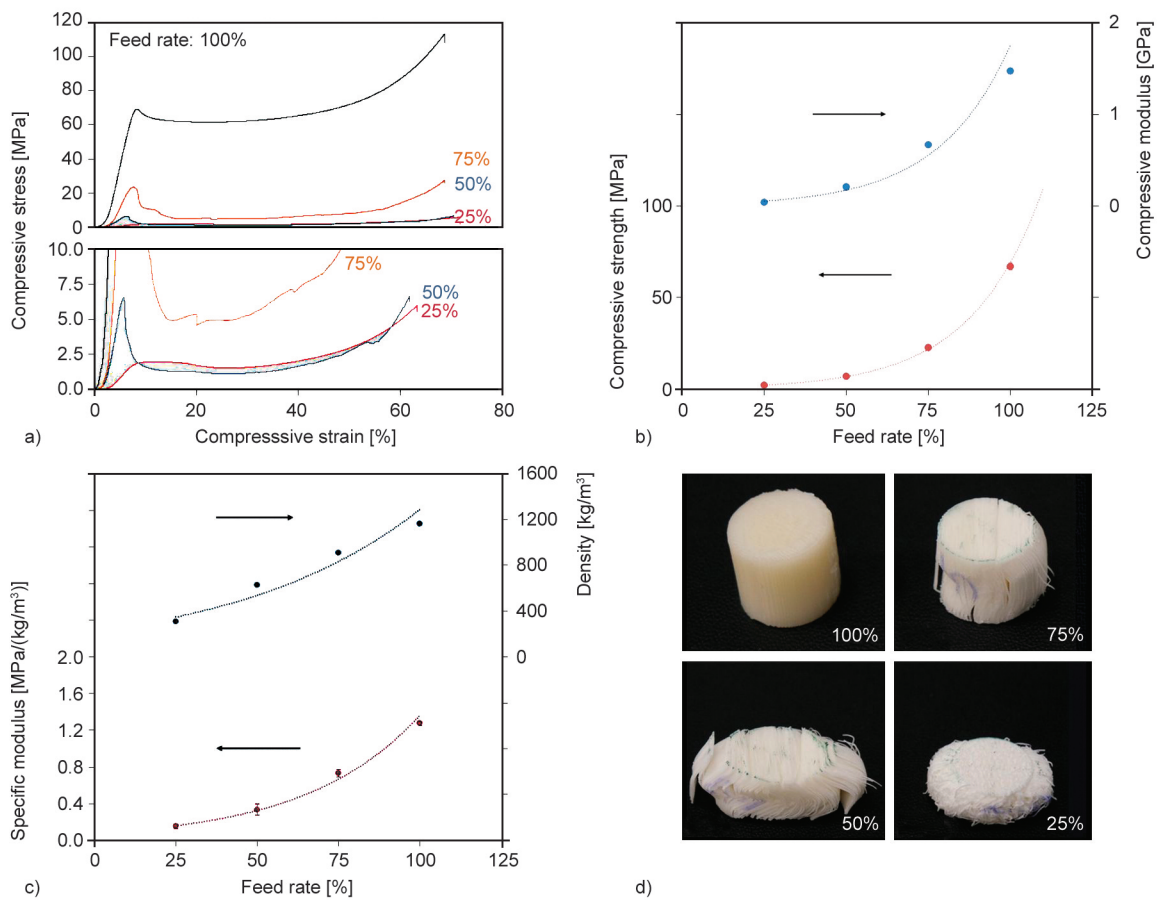


**Figure 14.** Effect of feed rate on the compressive mechanical properties. a) Representative compressive stress-strain curves of specimens printed using different feed rates. b) Compressive strength and elastic modulus as a function of feed rate. c) Specific elastic modulus and density as a function of feed rate. d) Photographs of compression specimens upon testing rate [%].

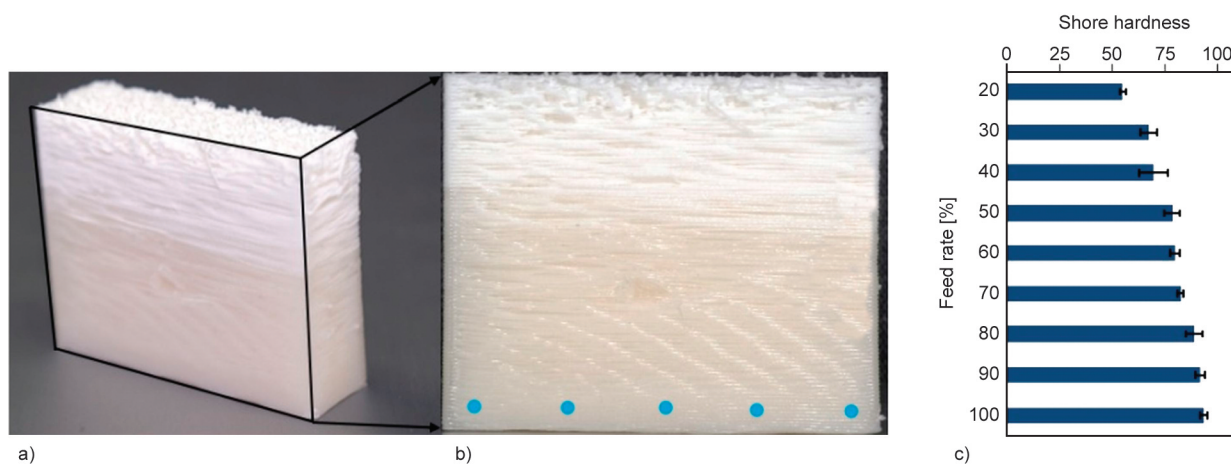


**Figure 15.** The Shore hardness measurements as a function of the feed rate and a photograph of the specimen. a) A photograph of the printed specimen with varying feed rates, b) front view of the specimen, where blue dots show the hardness measurement locations for the feed rate of 100% and c) Shore hardness over the thickness of the specimen. The error bar represents one standard deviation of five different measurements.

with an average feed rate of 20%, and it monotonically increases with feed rate, reaching 93.0 at a feed rate of 100%. The dependence of Shore hardness on feed rate is much smaller than those observed for tensile strength and compressive strength.

The specimen photographs suggest a reduction in the surface quality with decreasing feed rate. Further characterization of the surface properties would be necessary to implement such heterogeneous structures effectively in applications.

#### 4. Conclusions

This study investigated the mechanical properties of 3D-printed PLA foams under different printing parameters. The nozzle temperature, feed rate, and infill ratio significantly affect the extent of foaming, density, and mechanical properties. We can summarize the findings as follows:

- Increasing the nozzle temperature from 215 to 260°C increased foaming and decreased density by 40% and strength by 60%.
- Feed rate was also effective in tuning the foaming. By only adjusting the feed rate between 25 and 100%, it has been possible to achieve strength values in the range of 5 to 40 MPa.
- Infill ratio, printing speed, and layer thickness also influenced the foaming. However, these parameters are not practical for precise control of the density and strength due to their weak influence on foaming or the complicated trends involved.

- The Shore hardness strongly varied as a function of the feed rate. Decreasing the feed rate from 100 to 20% reduced the Shore hardness from 93.0 to 54.7. Nevertheless, this variation was less pronounced than those observed for tensile strength.

Foaming filaments provide additional control over printed parts' density and mechanical properties. With the capability to spatially control these properties, foaming filaments offer new opportunities for designing compliant mechanisms, soft robotics components, and biomedical scaffolds.

#### Acknowledgements

This work is funded by METU BAP under Project No. GAP-302-2021-10609. We would like to thank METU Central Laboratory and Mr. Servet Şehirli for their support in the testing and characterization.

#### References

- Zein I., Hutmacher D. W., Tan K. C., Teoh S. H.: Fused deposition modeling of novel scaffold architectures for tissue engineering applications. *Biomaterials*, **23**, 1169–1185 (2002).  
[https://doi.org/10.1016/S0142-9612\(01\)00232-0](https://doi.org/10.1016/S0142-9612(01)00232-0)
- Wimpenny D. I., Pandey P. M., Kumar J. L.: *Advances in 3D printing and additive manufacturing technologies*. Springer, Berlin (2017).  
<https://doi.org/10.1007/978-981-10-0812-2>
- Ngo T. D., Kashani A., Imbalzano G., Nguyen K. T. Q., Hui D.: Additive manufacturing (3D printing): A review of materials, methods, applications and challenges. *Composites Part B: Engineering*, **143**, 172–196 (2018).  
<https://doi.org/10.1016/j.compositesb.2018.02.012>

- [4] Bakır A. A., Atik R., Özerinç S.: Mechanical properties of thermoplastic parts produced by fused deposition modeling: A review. *Rapid Prototyping Journal*, **27**, 537–561 (2021).  
<https://doi.org/10.1108/RPJ-03-2020-0061>
- [5] Ben Ali N., Khlif M., Hammami D., Bradai C.: Mechanical and morphological characterization of spherical cell porous structures manufactured using FDM process. *Engineering Fracture Mechanics*, **216**, 106527 (2019).  
<https://doi.org/10.1016/j.engfracmech.2019.106527>
- [6] Choi W. J., Hwang K. S., Kwon H. J., Lee C., Kim C. H., Kim T. H., Heo S. W., Kim J.-H., Lee J.-Y.: Rapid development of dual porous poly(lactic acid) foam using fused deposition modeling (FDM) 3D printing for medical scaffold application. *Materials Science and Engineering: C*, **110**, 110693 (2020).  
<https://doi.org/10.1016/j.msec.2020.110693>
- [7] Sanz-Horta R., Elvira C., Gallardo A., Reinecke H., Rodríguez-Hernández J.: Fabrication of 3D-printed biodegradable porous scaffolds combining multi-material fused deposition modeling and supercritical CO<sub>2</sub> techniques. *Nanomaterials*, **10**, 1080 (2020).  
<https://doi.org/10.3390/nano10061080>
- [8] Damanpack A. R., Sousa A., Bodaghi M.: Porous PLAs with controllable density by FDM 3D printing and chemical foaming agent. *Micromachines*, **12**, 866 (2021).  
<https://doi.org/10.3390/mi12080866>
- [9] Lee S.-T., Park C. B.: *Foam extrusion: Principles and practice*. CRC Press, Ohio (2014).
- [10] Zhang X., Ding W., Chang E., Chen X., Chen J., Park C. B., Shen C.: Foaming behaviors and mechanical properties of injection-molded polylactide/cotton-fiber composites. *Industrial and Engineering Chemistry Research*, **59**, 17885–17893 (2020).  
<https://doi.org/10.1021/acs.iecr.0c03348>
- [11] Zhao H., Cui Z., Sun X., Turng L.-S., Peng X.: Morphology and properties of injection molded solid and microcellular polylactic acid/polyhydroxybutyrate-valerate (PLA/PHBV) blends. *Industrial and Engineering Chemistry Research*, **52**, 2569–2581 (2013).  
<https://doi.org/10.1021/ie301573y>
- [12] Dong G., Wijaya G., Tang Y., Zhao Y. F.: Optimizing process parameters of fused deposition modeling by Taguchi method for the fabrication of lattice structures. *Additive Manufacturing*, **19**, 62–72 (2018).  
<https://doi.org/10.1016/j.addma.2017.11.004>
- [13] Liu W., Song H., Wang Z., Wang J., Huang C.: Improving mechanical performance of fused deposition modeling lattice structures by a snap-fitting method. *Materials and Design*, **181**, 108065 (2019).  
<https://doi.org/10.1016/j.matdes.2019.108065>
- [14] Lee S.-T., Ramesh N. S.: *Polymeric foams: Mechanisms and materials*. CRC Press, Ohio (2004).
- [15] Wu G., Xie P., Yang H., Dang K., Xu Y., Sain M., Turng L. S., Yang W.: A review of thermoplastic polymer foams for functional applications. *Journal of Material Science*, **56**, 11579–11604 (2021).  
<https://doi.org/10.1007/s10853-021-06034-6>
- [16] Xu J., Turng L.-S.: *Microcellular injection molding*. Wiley, New Jersey (2010).
- [17] Ykhlef N., Lafranche E.: Development of bio-based poly(butylene succinate) formulations for microcellular injection foaming. *International Journal of Material Forming*, **12**, 1009–1022 (2019).  
<https://doi.org/10.1007/s12289-019-01512-4>
- [18] Gibson L. J., Ashby M. F.: *Cellular solids: Structure and properties*. Cambridge University Press, Cambridge (1997).
- [19] Kabir M. E., Saha M. C., Jeelani S.: Tensile and fracture behavior of polymer foams. *Materials Science and Engineering: A*, **429**, 225–235 (2006).  
<https://doi.org/10.1016/j.msea.2006.05.133>
- [20] Ramsteiner F., Fell N., Forster S.: Testing the deformation behaviour of polymer foams. *Polymer Testing*, **20**, 661–670 (2001).  
[https://doi.org/10.1016/S0142-9418\(00\)00090-8](https://doi.org/10.1016/S0142-9418(00)00090-8)
- [21] Ykhlef N., Lafranche E.: Injection-moulding of nitrogen-foamed bio-based microcellular poly(butylene succinate): Processing conditions/foam structure/flexural properties relationship. *Polymers from Renewable Resources*, **11**, 30–46 (2020).  
<https://doi.org/10.1177/2041247920952653>
- [22] Clifton W., Pichelmann M., Vlasak A., Damon A., Re-Faey K., Nottmeier E.: Investigation and feasibility of combined 3D printed thermoplastic filament and polymeric foam to simulate the cortiocancellous interface of human vertebrae. *Scientific Reports*, **10**, 2912 (2020).  
<https://doi.org/10.1038/s41598-020-59993-2>
- [23] Wallin T. J., Pikul J., Shepherd R. F.: 3D printing of soft robotic systems. *Nature Reviews Materials*, **3**, 84–100 (2018).  
<https://doi.org/10.1038/s41578-018-0002-2>
- [24] Zhai W., Hu B., Li M., Jiang J., Zhou M.: Dimensional accuracy control and compressive property of microcellular polyetherimide honeycomb foams manufactured by an *in situ* foaming fused deposition modeling technology. *Advanced Engineering Materials*, **23**, 2001449 (2021).  
<https://doi.org/10.1002/adem.202001449>
- [25] Li M., Jiang J., Hu B., Zhai W.: Fused deposition modeling of hierarchical porous polyetherimide assisted by an *in-situ* CO<sub>2</sub> foaming technology. *Composites Science and Technology*, **200**, 108454 (2020).  
<https://doi.org/10.1016/j.compscitech.2020.108454>
- [26] Marascio M. G. M., Antons J., Pioletti D. P., Bourbon P.-E.: 3D printing of polymers with hierarchical continuous porosity. *Advanced Materials Technologies*, **2**, 1700145 (2017).  
<https://doi.org/10.1002/admt.201700145>

- [27] Zhou C., Yang K., Wang K., Pei X., Dong Z., Hong Y., Zhang X.: Combination of fused deposition modeling and gas foaming technique to fabricated hierarchical macro/microporous polymer scaffolds. *Materials and Design*, **109**, 415–424 (2016).  
<https://doi.org/10.1016/j.matdes.2016.07.094>
- [28] Song P., Zhou C., Fan H., Zhang B., Pei X., Fan Y., Jiang Q., Bao R., Yang Q., Dong Z., Zhang X.: Novel 3D porous biocomposite scaffolds fabricated by fused deposition modeling and gas foaming combined technology. *Composites Part B: Engineering*, **152**, 151–159 (2018).  
<https://doi.org/10.1016/j.compositesb.2018.06.029>
- [29] Kaygusuz B., Özerinç S.: Improving the ductility of polylactic acid parts produced by fused deposition modeling through polyhydroxyalkanoate additions. *Journal of Applied Polymer Science*, **136**, 48154 (2019).  
<https://doi.org/10.1002/app.48154>
- [30] Camargo J. C., Machado Á. R., Almeida E. C., Silva E. F. M. S.: Mechanical properties of PLA-graphene filament for FDM 3D printing. *The International Journal of Advanced Manufacturing Technology*, **103**, 2423–2443 (2019).  
<https://doi.org/10.1007/s00170-019-03532-5>
- [31] Camargo J. C., Machado A. R., Almeida E. C., de Almeida V. H. M.: Mechanical and electrical behavior of ABS polymer reinforced with graphene manufactured by the FDM process. *The International Journal of Advanced Manufacturing Technology*, **119**, 1019–1033 (2022).  
<https://doi.org/10.1007/s00170-021-08288-5>
- [32] Colorfabb: Technical data sheet for LW-PLA filament.
- [33] ASTM D638-4: Standard test method for tensile properties of plastics – Tension (2021).
- [34] ASTM D1621: Standard test method for compressive properties of rigid cellular plastics – Compression (2016).
- [35] ASTM D2240: Standard test method for rubber property – Durometer hardness (2021).
- [36] Tsvintzelis I., Angelopoulou A. G., Panayiotou C.: Foaming of polymers with supercritical CO<sub>2</sub>: An experimental and theoretical study. *Polymer*, **48**, 5928–5939 (2007).  
<https://doi.org/10.1016/j.polymer.2007.08.004>
- [37] Bakır A. A., Atik R., Özerinç S.: Effect of fused deposition modeling process parameters on the mechanical properties of recycled polyethylene terephthalate parts. *Journal of Applied Polymer Science*, **138**, 49709 (2021).  
<https://doi.org/10.1002/app.49709>
- [38] Ameli A., Jahani D., Nofar M., Jung P. U., Park C. B.: Development of high void fraction polylactide composite foams using injection molding: Mechanical and thermal insulation properties. *Composites Science and Technology*, **90**, 88–95 (2014).  
<https://doi.org/10.1016/j.compscitech.2013.10.019>
- [39] Radhakrishna G., Dugad R., Gandhi A.: Morphological evaluation of microcellular foamed composites developed through gas batch foaming integrating fused deposition modeling (FDM) 3D printing technique. *Cellular Polymers*, **40**, 244–266 (2021).  
<https://doi.org/10.1177/02624893211040938>
- [40] Aliheidari N., Tripuraneni R., Hohimer C., Christ J., Ameli A., Nadimpalli S.: The impact of nozzle and bed temperatures on the fracture resistance of FDM printed materials. in ‘Proceedings of Behavior and Mechanics of Multifunctional Materials and Composites. Oregon, United States’ Vol. **10165**, 1016512 (2017).  
<https://doi.org/10.1117/12.2260105>
- [41] Puerta A. P. V., Fernandez-Vidal S. R., Batista M., Girot F.: Fused deposition modelling interfacial and interlayer bonding in PLA post-processed parts. *Rapid Prototyping Journal*, **26**, 585–592 (2019).  
<https://doi.org/10.1108/RPJ-06-2019-0176>
- [42] Fernandez-Vicente M., Calle W., Ferrandiz S., Conejero A.: Effect of infill parameters on tensile mechanical behavior in desktop 3D printing. *3D Printing and Additive Manufacturing*, **3**, 183–192 (2016).  
<https://doi.org/10.1089/3dp.2015.0036>
- [43] Nuñez P. J., Rivas A., García-Plaza E., Beamud E., Sanz-Lobera A.: Dimensional and surface texture characterization in fused deposition modelling (FDM) with ABS plus. *Procedia Engineering*, **132**, 856–863 (2015).  
<https://doi.org/10.1016/j.proeng.2015.12.570>
- [44] Ameli A., Jahani D., Nofar M., Jung P. U., Park C. B.: Processing and characterization of solid and foamed injection-molded polylactide with talc. *Journal of Cellular Plastics*, **49**, 351–374 (2013).  
<https://doi.org/10.1177/0021955X13481993>
- [45] Kanani A. Y., Rennie A. E. W., Abd Rahim S. Z. B.: Additively manufactured foamed polylactic acid for lightweight structures. *Rapid Prototyping Journal*, in press (2022).  
<https://doi.org/10.1108/RPJ-03-2022-0100>
- [46] Soud W., Baqer I. A., Ahmed M.: Experimental study of 3D printing density effect on the mechanical properties of the carbon-fiber and polylactic acid specimens. *Engineering and Technology Journal*, **37**, 128–132 (2019).  
<https://doi.org/10.30684/etj.37.4A.3>
- [47] Farah S., Anderson D. G., Langer R.: Physical and mechanical properties of PLA, and their functions in widespread applications – A comprehensive review. *Advanced Drug Delivery Reviews*, **107**, 367–392 (2016).  
<https://doi.org/10.1016/j.addr.2016.06.012>
- [48] Calvert K. L., Trumble K. P., Webster T. J., Kirkpatrick L. A.: Characterization of commercial rigid polyurethane foams used as bone analogs for implant testing. *Journal of Materials Science: Materials in Medicine*, **21**, 1453–1461 (2010).  
<https://doi.org/10.1007/s10856-010-4024-6>